

Physical virology

W. H. Roos¹*, R. Bruinsma² and G. J. L. Wuite¹*

Viruses are nanosized, genome-filled protein containers with remarkable thermodynamic and mechanical properties. They form by spontaneous self-assembly inside the crowded, heterogeneous cytoplasm of infected cells. Self-assembly of viruses seems to obey the principles of thermodynamically reversible self-assembly but assembled shells ('capsids') strongly resist disassembly. Following assembly, some viral shells pass through a sequence of coordinated maturation steps that progressively strengthen the capsid. Nanoindentation measurements by atomic force microscopy enable tests of the strength of individual viral capsids. They show that concepts borrowed from macroscopic materials science are surprisingly relevant to viral shells. For example, viral shells exhibit 'materials fatigue' and the theory of thin-shell elasticity can account — in part — for atomic-force-microscopy-measured force-deformation curves. Viral shells have effective Young's moduli ranging from that of polyethylene to that of plexiglas. Some of them can withstand internal osmotic pressures that are tens of atmospheres. Comparisons with thin-shell theory also shed light on nonlinear irreversible processes such as plastic deformation and failure. Finally, atomic force microscopy experiments can quantify the mechanical effects of genome encapsidation and capsid protein mutations on viral shells, providing virological insight and suggesting new biotechnological applications.

The impact of viruses on our daily lives is dominated by their role as infectious agents of, often serious, diseases. However, viruses are now increasingly employed in more positive roles^{1,2}. Examples include viruses and viral shells that are used in batteries and memory devices^{3,4}, as nanoscaffolds or nanoreactors for transport and catalysis^{5,6}, and in cancer treatment⁷. In the context of gene therapy, they are used as vectors for gene delivery⁸, and the 'phage' viruses that infect bacteria have been used as antibacterial agents⁹. Supporting these applications is the burgeoning research field of physical virology dedicated to the study of the physical properties of viruses¹⁰. It encompasses domains such as viral self-assembly^{11,12}, virus genome packaging and release mechanisms^{13–15}, and structural and mechanistic studies of viral particles^{14,16,17}. The rapid growth of this field is, on the one hand, fuelled by the development of physics-based techniques such as cryo-electron microscopy, X-ray crystallography, optical tweezers and atomic force microscopy and, on the other hand, by the increasing interest in viral particles as 'smart' building blocks of larger-scale structures. In this brief review we shall focus on just two aspects of physical virology: first what physics has to tell us about the assembly of viral shells, and second what the mechanical properties of assembled viral shells are: how we can experimentally probe mechanical properties of viral shells, how we should interpret them and how we can apply the insights these studies provide.

Viral self-assembly

Viruses do not carry out metabolic activity and rely entirely on host-cell molecular machinery for reproduction. This absence of metabolic and reproductive activity suggests that, unlike cells, the assembly of viruses could perhaps be understood on the basis of equilibrium thermodynamics. An elegant confirmation of this idea was the discovery in 1955 by Fraenkel-Conrat and Williams^{18,19} that under *in vitro* conditions the rod-like tobacco mosaic virus (TMV) self-assembles spontaneously and unassisted into fully infectious viral particles from solutions containing the molecular components of this virus: the TMV capsid proteins (or 'subunits') and the single-stranded (ss) RNA genome molecules of TMV. In 1967, Bancroft, Hills and Markham²⁰ showed that

small sphere-like plant viruses with icosahedral symmetry also can be produced by *in vitro* self-assembly (Box 1 summarizes the general classification of viruses with icosahedral viral symmetry). The connection between equilibrium thermodynamics and viral self-assembly was further strengthened by the work of Klug²¹, who determined the thermodynamic phase diagram of solutions of TMV subunits in terms of acidity and salinity. Capsid proteins, or 'subunits', interact mainly through a combination of electrostatic repulsion, hydrophobic attraction and specific contacts between certain pairs of amino acids (known as 'Caspar pairs'²²). Varying the acidity and salinity conditions (or the concentration of Ca²⁺ ions) adjusts the relative balance between these competing interactions, thereby favouring assembly or disassembly²³ of protein aggregates. For TMV subunits in ambient conditions of acidity–salinity–temperature the most stable subunit aggregates are 'double-disc' and 'double-ring' protein clusters held together by hydrophobic attractive interactions. Electrostatic repulsion between the positively charged discs/rings prevents disc aggregation. The addition of the oppositely charged ssRNA genome molecules drives the self-assembly process to completion by combining the protein discs into rod-like cylinders with the RNA molecule running along the central axis, like beads on a string²¹. Self-assembly of most infectious sphere-like ssRNA viruses under ambient conditions requires the presence of the viral RNA genome molecules. Viral RNA molecules act in part as a non-specific 'electrostatic glue' that links together the oppositely charged capsid proteins²⁴, and particular 'stem-loop' side branches of the RNA molecules have specific affinity for the capsid proteins. In some cases, the encapsidated ssRNA molecules condense as double-stranded (ds) helical segments along a dodecahedral cage of edges of the icosahedral shell²⁵. Self-assembly of empty capsids in the absence of RNA may be possible as well for certain viruses, for instance under non-ambient pH or salinity levels. On the other hand, self-assembly of viral shells of most ds genomes, such as the tailed dsDNA 'bacteriophage' viruses (that is, viruses that prey on bacteria), does not require the presence of genome molecules. The much larger bending rigidity of dsDNA molecules presumably prevents them from acting as 'electrostatic glue'.

¹Natuur- en Sterrenkunde & Laser Centrum, VU University, De Boelelaan 1081, 1081 HV Amsterdam, The Netherlands, ²Department of Physics, University of California, Los Angeles, California 90095-1537, USA. *e-mail: wroos@few.vu.nl; gwuite@nat.vu.nl

Box 1 | Viral shapes.

Viral particles come in many shapes, of which sphere-like and rod-like particles are the most common, but spherocylinders, cones and other shell shapes are seen as well. About half of all viral families share icosahedral symmetry, even when the viral genomes share little homology⁹². Examples include the plant virus CCMV, the animal virus HBV and bacteriophage viruses discussed in this review. Caspar and Klug (CK) developed a classification system for icosahedral viruses, illustrated in Fig. B1, based on the ‘*T* number’ defined as $T = m^2 + n^2 + mn$. Here, m and n indicate the number of steps along the crystallographic directions of a hexagonal lattice connecting two adjacent vertices on the icosahedron^{93,94}. A CK icosahedral shell consists of 12 pentamers located at equidistant sites on the icosahedral vertices with a further $10(T - 1)$ hexamers — with $T = 1, 3, 4, 7, \dots$ — located in between the pentamers. Following earlier work by Crick and Watson⁹⁵, CK argued that this type of icosahedral shell minimizes the geometrically unavoidable elastic strains of identical proteins placed on a closed shell (‘quasi-equivalence’).

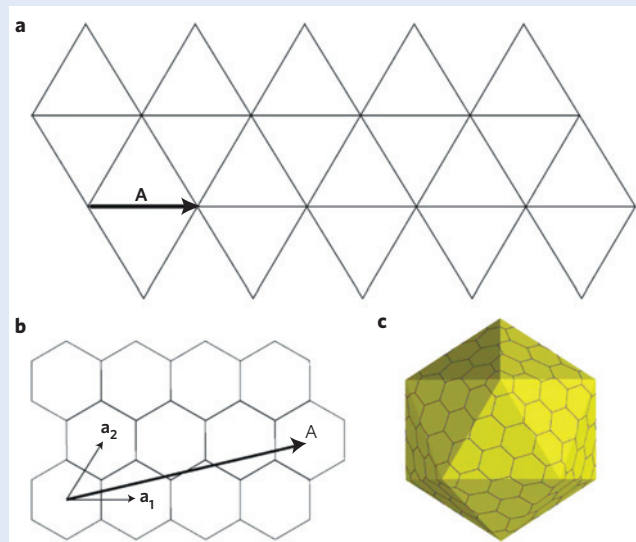


Figure B1 | Caspar and Klug construction of icosahedral viral shells.

a, Template — consisting of equilateral triangles — of which an icosahedron can be folded. The lattice vector $\mathbf{A} = m\mathbf{a}_1 + n\mathbf{a}_2$ of a hexagonal lattice with basis vectors \mathbf{a}_1 and \mathbf{a}_2 forms an index for the triangles. **b**, An example for $m = 3$ and $n = 1$. **c**, Result of folding a template with this lattice vector into an icosahedron. It has a $T = m^2 + n^2 + mn = 13$ structure with $10(T - 1) = 120$ hexamers in total. Reproduced with permission from ref. 48, © 2005 APS.

In these cases, the genome is usually inserted, after capsid assembly has been completed, by the action of a rotary molecular motor imbedded in the capsid¹⁵.

Assembly studies by the group of Zlotnick of the assembly of two icosahedral viruses — cowpea chlorotic mottle virus (CCMV; ref. 26) and hepatitis B virus (HBV; ref. 27) — were an important milestone for the application of equilibrium thermodynamics. They measured the concentrations of subunit clusters of different sizes as a function of the total protein concentration and encountered a double-peaked population composed of, respectively, small clusters (for example, dimers or pentamers) and fully formed capsids. The surprise was that the ratio of the concentrations of free subunits and fully formed capsids seemed to obey quantitatively the law of mass action (LMA). The LMA would demand that for a viral

shell composed of N subunits the concentration of assembled capsids should be proportional to ϕ^N , with ϕ the concentration of free subunits, which must be distinguished from the total protein concentration ϕ_T . An important consequence of the LMA is the fact that, as a function of ϕ_T , the fraction $f(\phi_T)$ of proteins incorporated into capsids rises sharply at a quasi-critical concentration ϕ_{crit} with $f(\phi_T) \sim 1 - \phi_{crit}/\phi_T$ for $\phi_T > \phi_{crit}$. As, according to the LMA, the value of $\phi_{crit} \propto \exp(\beta \Delta G_0/N)$ is determined by the ‘standard Gibbs free energy’ ΔG_0 of the assembly reaction, that is, the assembly free energy of the capsid, important thermodynamic information can be obtained by measuring ϕ_{crit} . This form for $f(\phi_T)$ fits very well the equilibrium self-assembly curves of, for example, micelles (‘critical micelle concentration’)²⁸. It describes quite well the self-assembly of CCMV and HBV with a ϕ_{crit} typically in the μM range. Under biological conditions, inside infected cells, the concentration of capsid proteins produced by transcription would thus have to exceed ϕ_{crit} before viral self-assembly could start. Fitted values for ΔG_0 were in the reasonable range of about $10 k_B T$ per subunit, so in total about $10^3 k_B T$ for small viral shells. The measured dependence of the fitted ΔG_0 on pH and salinity was also consistent with simple models for the interactions between subunits²³. The LMA is a direct consequence of the minimization of the Gibbs free energy: it requires that capsid proteins in solution have the same chemical potential as the proteins incorporated in a shell. However, when the total concentration of capsid proteins is reduced back down below ϕ_{crit} after the assembly has reached completion, then capsids should disassemble spontaneously according to the LMA. In actuality this either does not happen at all, or happens only after a very long period of time, or after quite substantial changes in pH, salinity or other solution conditions²⁹. This ‘excess’ thermodynamic stability of assembled viral shells when compared with conventional equilibrium self-assembly is, from a biological viewpoint, of course a prime ‘survival’ feature, as viral shells need to remain intact in ‘hostile’ environments that contain no free capsid proteins at all, such as the host bloodstream, stomach or tissue. This means that viral self-assembly really should not be viewed as an equilibrium process. Analytical and numerical studies³⁰ of simple models of capsid assembly kinetics³¹ indicate that provided most assembly steps are reversible, with one or a few assembly steps irreversible, an LMA-type double-peaked distribution obeying $f(\phi_T) \sim 1 - \phi_{crit}/\phi_T$ will still develop under certain conditions. However, the ‘ ΔG_0 ’ extracted from this ϕ_{crit} in general is considerably smaller than the actual standard free energy of the capsid, and reflects the assembly free energy of reversible intermediate structures.

Kinetic studies of viral self-assembly would be necessary to probe this limited form of irreversibility but, unlike the case of the rod-like TMV, it has turned out to be very challenging to identify experimentally the assembly intermediates of spherical viruses. Kinetic studies of viral assembly by electron microscopy carried out in the 1980s on brome mosaic virus (BMV) assembly reported partially formed shells³². In 1993, the group of Prevelige studied the kinetics of scaffold-based assembly of the phage P22 using light scattering³³. Capsid assembly was shown to be preceded by a lag time after initiation followed by a more rapid sigmoidal growth curve, indicating that the capsid-assembly rate is determined by nucleation. A critical protein concentration is required below which assembly does not take place. The initial formation rate depended on the protein concentration to the fifth power, which suggests that in this case pentamers are the critical nuclei. RNA genome molecules have been shown to catalyse the assembly process by assisting the formation of the critical nucleus of BMV (ref. 34). Subsequent capsid growth seems to be sequential, resembling a polymerization reaction. Studies of the assembly kinetics of a number of viruses have reported similar scenarios, with lag times in the seconds–minutes range³⁵. Particularly detailed was a multi-angle light-scattering study by

Casini *et al.*³⁶ of the assembly kinetics of human papilloma virus; they again found that the rate-limiting step of the assembly process was the formation of protein oligomers.

Numerical simulations of viral assembly kinetics could complement assembly-kinetics experiments. However, simulations on the relevant timescale of seconds to minutes that account for the internal degrees of freedom of capsid proteins interacting through realistic potentials are, for currently available computational resources, not practical. Instead, rigid geometrical models of the capsid proteins (or capsomeres) and other coarse-grained representations are used, with the model proteins/capsomeres interacting through some model pair potential^{37–42}. In the simplest case, capsid proteins or capsomeres could even be represented as point particles. A Newtonian-dynamics study by Hagan and Chandler⁴¹ of such a model reported that the choice of this pair potential sensitively determined whether ‘kinetic traps’ prevented proper assembly of small shells. Hicks and Henley⁴² used an elastic model, with the proteins now represented as deformable triangles, and found that the probability for successful assembly of larger shells rapidly decreased when the elastic rigidity was increased. An example of an assembly error could be a five-fold-symmetric capsomere inserted at a location that is not appropriate for an icosahedral shell (see Box 1). More recently, molecular dynamics (MD) simulations of viral assembly have been carried out where the capsomeres/proteins were represented by more realistic geometrical shapes. MD simulations by Nguyen, Reddy and Brooks⁴³ were able to reproduce the self-assembly of smaller $T = 1$ and $T = 3$ shells. They found though that proper assembly was accompanied by the production of significant numbers of non-icosahedral ‘aberrant’ particles associated with assembly errors and kinetic traps, in particular when temperature and protein concentrations were not optimally chosen. Next, Rapaport⁴⁴ included explicit solvent molecules and succeeded in assembling $T = 1$ particles with a high level of fidelity and sigmoidal assembly kinetics. The high levels of assembly fidelity in this case seemed to be characterized by high levels of assembly reversibility. Recall that high levels of assembly reversibility were also required for the observed quasi-LMA. A ‘local-rule’ scheme has been proposed⁴⁵, engineered to prevent the assembly-error problem by assuming that viral proteins can adopt T different internal configurations ‘coding’ for proper assembly of an icosahedral shell with index T (see Box 1). So far, no evidence has been found for local-rule-based coding configurations.

If only the minimum-free-energy state of a shell is required then viral shell assembly also can be studied by Monte Carlo simulations. A ‘two-disc’ Monte Carlo simulation by Zandi *et al.*, representing pentamers and hexamers placed on a spherical support scaffold, found that the Caspar and Klug (CK) T -number icosahedral symmetry is indeed the minimum-free-energy structure provided that the size ratio of the discs is fixed appropriately⁴⁶. Chen, Zhang and Glotzer⁴⁷ investigated cluster formation of attractive cone-shaped particles without support scaffold using Monte Carlo simulation. By varying the cone angle they found that the cones assembled into a sequence of convex shells characterized by ‘magic numbers’ that included the icosahedral shells. Non-icosahedral shell structures, like those of human immunodeficiency virus (conical) and of phage $\Phi 29$ (prolate/spherocylinder), can be obtained as minimum-energy structures for certain parameter ranges in elastic-shell models⁴⁸. Design principles of prolate phages were reviewed by Moody⁴⁹ in 1999. Monte Carlo simulations of the packing of hard spheres on a prolate, spheroidal surface identified the minimal requirements to form shells resembling those of a few selected viruses⁵⁰, and Monte Carlo simulations of capsomere–capsomere interactions in prolate shells yielded optimal structures for particles with icosahedral end caps connected by cylinders of hexamers⁵¹. Finally, the capsids of many animal viruses,

such as human immunodeficiency virus (HIV), HBV and herpes simplex virus, are surrounded by a lipid bilayer envelope, and Zhang and Nguyen studied the effect of this lipid bilayer on the nucleation of the cone-shaped HIV shells⁵².

After the initial assembly of a virus, the capsid proteins are often modified, a process known as maturation. For example, the capsids of many tailed dsDNA bacteriophages undergo a whole sequence of conformational changes and chemical reactions that tend to strengthen the shell, which is necessary in part because of the large internal pressure of phages, which is discussed later on. The shell-maturation steps, which have been shown to be cooperative in certain cases, resemble structural phase transitions in crystals. The application of Ginzburg–Landau theory to describe the maturation steps indicates that near a step we could expect to encounter the same ‘soft modes’ as characterize structural transitions⁵³. An exceptional case is the bacteriophage HK97, where, after an elaborate sequence of steps, the shell ends up being armoured by a cross-linked mesh of amino-acid chains that has the topology of medieval chain-mail⁵⁴. Tama and Brooks^{55,56} carried out all-atom numerical studies of some of the maturation steps of HK97 and found that the conformational changes of the shell do indeed tend to follow the trajectory of soft modes of the shell, associated with rotation of the pentamers and hexamers. Widom *et al.* used the continuum elasticity theory of thin shells to show that, even in the absence of internal protein conformational degrees of freedom driving the maturation, icosahedral shells should still exhibit soft modes near the buckling transition between spherical and icosahedral shapes⁵⁷. Finally, Yang *et al.*⁵⁸ showed that the same theory could account for the low-frequency modes of the shells of simple viruses such as BMV.

Mechanical virology

After a virus or an empty viral shell has assembled, we can inquire how resilient it is in terms of its response to external force and other perturbations. Capsids need to meet conflicting demands: they should be sufficiently stable to protect their genome in the extracellular environment, but sufficiently unstable that they can release their genome molecules into host cells. Various bulk and single-particle assays have been developed to measure the mechanical properties of viruses, the budding field of mechanical virology. Osmotic-shock experiments were used to study the stability of bacteriophage viruses under pressure against rupture^{14,59} and the mechanical properties of crystals and films composed of viruses were analysed by Brillouin light scattering^{60,61}. A disadvantage of these multiparticle techniques is that (1) they represent an average over large numbers of viruses and (2) they represent a rotational average, so any directionality of the mechanical properties with respect to the shell orientation is lost. The mechanics of single particles and their directionality can however be probed with the atomic force microscopy (AFM-) based nanoindentation techniques summarized in Box 2.

The relation between the applied force and the resulting change in shell diameter is called the force–deformation curve (FDC; see Box 2). Depending on whether or not the capsid returns to its original state after the probe force is removed (‘unloading’), we call this a reversible, respectively irreversible, deformation. The force measured by a nanoindentation probe results, at a fundamental level, from the fact that the probe forces the viral shell away from a state of minimum free energy. To interpret measured FDCs, including irreversibility effects, we can compare them with the deformation free energy obtained from the continuum elasticity theory of thin elastic shells (‘thin-shell theory’ or TST) that we have already mentioned. TST is used extensively by engineers to predict the effects of external forces on thin-walled, hollow macroscopic structures, such as aeroplanes or oil tanks. In the simplest application of TST we model a viral shell as a thin spherical

Box 2 | AFM nanoindentation.

The mechanical properties of various biological entities have been characterized by AFM-based nanoindentation⁹⁶, including cells^{97,98}, microtubules^{99,100}, peptide nanotubes¹⁰¹ and viruses^{67,79}. Figure B2 shows a schematic diagram of a nanoindentation experiment on a virus. The experiments can be carried out in air as well as in liquid. The minimal radius of curvature of commercial AFM tips is $\sim 2\text{--}20$ nm, a value that is, respectively, a little lower than or comparable to the size of small viruses. Before the start of a nanoindentation experiment, the viral particle needs to be imaged^{102,103} to check whether it has the correct shape and size (Fig. B3a). Viral imaging under liquid conditions in combination with mechanical probing has been carried out in tapping-mode¹⁰⁴ and jumping-mode¹⁰⁵ AFM, two relatively non-invasive imaging modes, which is of importance for the imaging of fragile biological structures such as icosahedral viruses. The more rigid, rod-like viruses have been imaged in contact-mode AFM without inducing visible damage⁶⁹. Imaging is followed by indentation of the virus, during which a force–distance curve (FZC) is recorded. This

FZC involves the bending of two springs in series, the cantilever and the viral particle. For this reason, a calibration FZC of the cantilever deflection on the solid substrate next to the virus must be recorded. From these two FZCs the FDC of the virus can be determined, showing the force as a function of the indentation of the virus (Fig. B2b,d). The schematic FDC of Fig. B2d shows an initially linear deformation regime with positive slope, for forces up to 1.7 nN, that is fully reversible. The slope of a linear, reversible indentation curve yields the particle's 'spring constant' and Young's modulus, as discussed in the text. This is followed by a deformation regime with negative slope, which is usually irreversible. This drop in force can indicate buckling of the shell or fracture of the shell ('failure'). Figure B3 shows a viral particle before and after a nanoindentation experiment. A hole produced by shell failure is clearly visible. Note that individual capsomeres are discernible. By comparing the image before and after indentation, the capsomeres that were removed by the indentation can be identified.

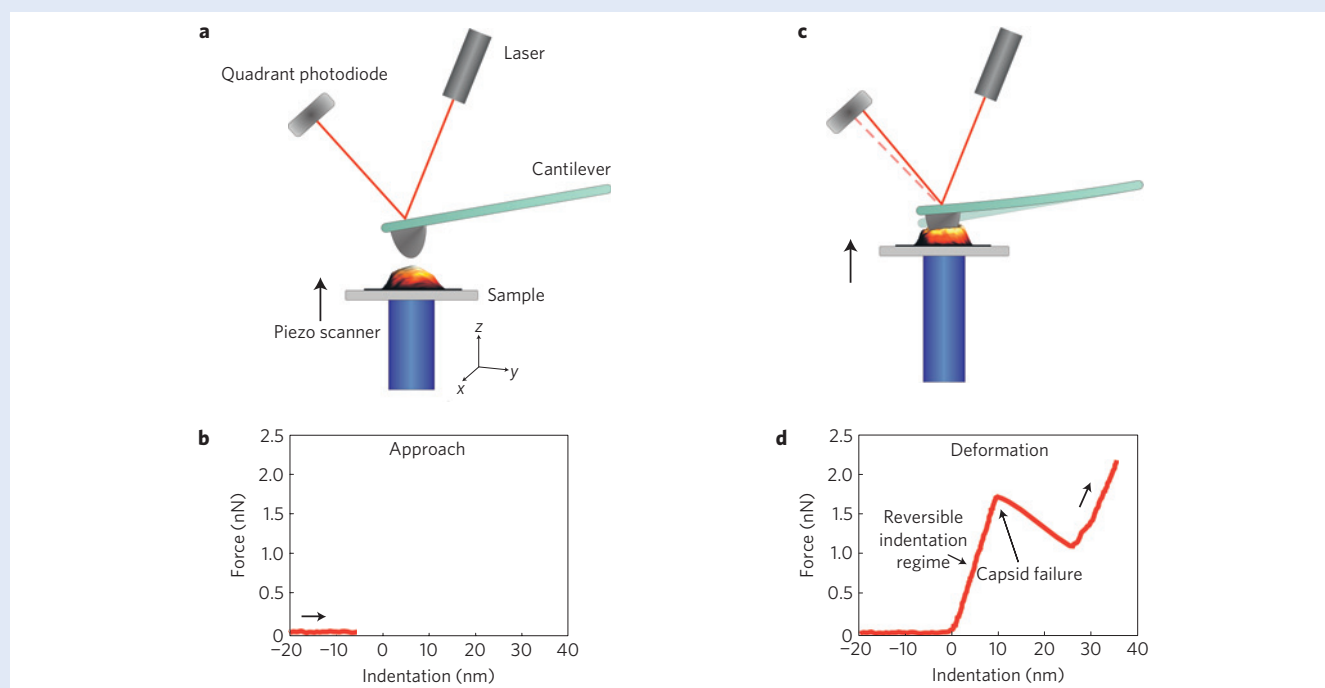


Figure B2 | Schematic diagram of AFM nanoindentation. **a,b**, The piezo is extending in **a**, but the AFM tip has not yet touched the virus surface and therefore the exerted force is zero (**b**). **c,d**, The AFM tip is indenting the virus and the cantilever bends (**c**); the change in signal on the quadrant photodiode is a measure for the exerted force, plotted in **d** as a function of the indentation.

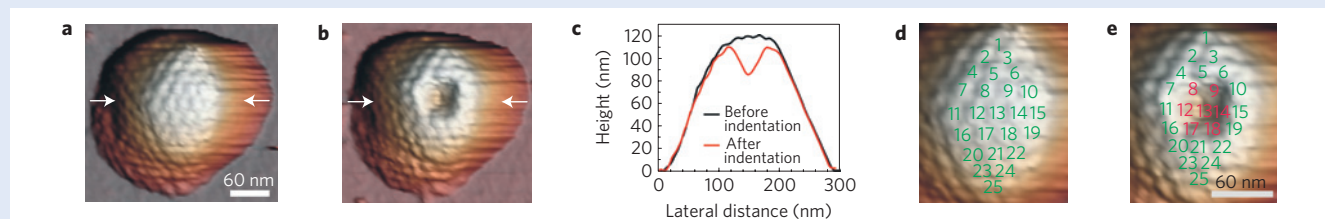


Figure B3 | AFM images of a single viral particle before and after nanoindentation. **a,b**, Three-dimensional rendered AFM topography images of a liquid-immersed HSV1 particle before (**a**) and after (**b**) indentation. The structural subunits (capsomeres) can be recognized on the viral shell. **c**, The height profile, taken along the white arrows in **a** and **b**, shows the capsomeres on top of the particle before indentation and the hole left after indentation. The indented profile most probably represents the tip shape and because of the finite width of the AFM tip it was not possible to image inside the broken capsid. **d,e**, Numbering of the capsomeres before and after indentation reveals the removal of seven (denoted in red) central capsomeres as a result of shell failure. Reproduced with permission from ref. 65, © 2009 NAS, USA.

shell of uniform thickness and radius R . If the viral shell encloses genome molecules, then an internal osmotic pressure Π must be included, which can be as large as ~ 50 atm (refs 62,63). Let $\zeta(\mathbf{r})$ be the indentation profile of the shell generated, for example, by a force probe. Specifically, $\zeta(\mathbf{r})$ is defined as the radial inward displacement of the surface of the sphere expressed in terms of a two-dimensional coordinate system that covers the shell. In the limit of small $\zeta(\mathbf{r})$, the TST deformation free energy ΔF is a simple functional of $\zeta(\mathbf{r})$ in the form of an integral over the shell surface:

$$\Delta F = \int dS \left\{ \frac{1}{2} \kappa (\Delta \zeta)^2 + \frac{1}{2} \tau (\nabla \zeta)^2 + \frac{1}{2} Y \left(\frac{2\zeta}{R} \right)^2 \right\} \quad (1)$$

The first term of equation (1) describes the bending-energy cost of the indentation — note that $\Delta \zeta$ is the shell curvature — where the bending modulus κ has units of energy. The second term represents the work by the probe against the genome osmotic pressure Π with $\tau = \Pi R/2$ an effective surface tension. The third term measures the stretching of the layer induced by the force with the two-dimensional Young modulus Y of the layer. A dimensionless number $\gamma = YR^2/\kappa$ — the Föppl–von Kármán number — and a characteristic length scale $l_b = \sqrt{\kappa/Y}$ — the buckling radius — can be constructed from the stretching and bending moduli, which will play an important role. For example, equation (1) is valid only if $\zeta^2 \ll l_b^2$. The FDC must be obtained from the thermodynamic condition that the functional derivative $\delta \Delta F / \delta \zeta(\mathbf{r})$ of the deformation free energy with respect to $\zeta(\mathbf{r})$ is equal to the radial force per unit area $f(\mathbf{r})$ exerted by the probe. The differential equation $\delta \Delta F / \delta \zeta(\mathbf{r}) = f(\mathbf{r})$ can be solved analytically for the case of a point force $f(\mathbf{r}) = F\delta(\mathbf{r})$. The force creates a dimple with a radius of order $\sqrt{Rl_b}$ and the resulting FDC is linear. In other words, for weak applied forces, the shell behaves like a harmonic spring. For zero osmotic pressure, for example, $\zeta(0)/R = F/8\sqrt{\kappa Y}$, in which case the effective spring constant is $k = 8\sqrt{\kappa Y}/R$. Alternatively, we can also apply three-dimensional elasticity theory to compute the elastic response of an elastic shell with a finite thickness h . We recover the TST result in the limit $h \ll R$ with a spring constant

$$k \propto E_{3D} h^2 / R \quad (2)$$

where E_{3D} is the three-dimensional Young modulus. For larger indentation forces equations (1) and (2) should not be used. The calculation of the FDC of TST in the nonlinear regime requires the solution of a pair of somewhat challenging nonlinear differential equations, known as the Föppl–von Kármán (FvK) equations (they resemble Einstein’s equations of general relativity). Instead of trying to solve the FvK equations analytically or numerically, it is more practical to numerically minimize the elastic energy directly using finite-element modelling (FEM). The inset of Fig. 1b shows the fully nonlinear FDC of a shell indented by a hemispherical tip as computed by FEM. The initial state was a uniform sphere. The FDC is plotted as a dimensionless relation between $\zeta(0)/R$ and $F/\sqrt{\kappa Y}$. Note that the deformation of the sphere does not deviate much from the linear harmonic spring for deformation ratios $\zeta(0)/R$ up to 0.6. Then, for slightly larger values of $\zeta(0)/R$, a discontinuous drop takes place in the FDC. This is due to the fact that for larger deformations the elastic energies of two different shapes of the deformed shell cross each other. In the engineering literature, singularities in the FDC of this type are known as ‘buckling’ transitions. They are identified with the well-known catastrophic failures of hollow structures subject to external loads, that is, failures without any visible precursor ‘warning’ in the FDC.

Comparison with the FDC of Box 2 suggests a relation between the buckling instabilities of TST and the irreversible nonlinearities

of the FDCs of viral shells. However, mathematically, the buckling discontinuities of TST are quite similar to first-order phase transitions and, like first-order phase transitions, they could be nucleated by local structural defects. This indicates that the elastic response of the non-uniform icosahedral shells might differ from that of uniform spherical shells, which must be discussed before we can compare with experiment. The FDC of icosahedral shells was obtained by starting from a perfect icosahedron as the initial trial state. The sharp folds linking the 12 vertices of a perfect icosahedron are not compatible with the bending-energy term in equation (1). However, as long as the FvK parameter $\gamma = YR^2/\kappa$ exceeds a threshold value of the order of 10^2 , the minimum-free-energy shape still remains icosahedrally faceted. For FvK numbers less than this threshold, however, the shell adopts a nearly spherical shape⁶⁴ (confusingly, this also is known as a buckling transition, but we shall not use this terminology). The FvK number of a viral shell can be estimated by comparing computed shapes of undeformed shells with those measured, for example, by cryo-transmission electron microscopy. Figure 1b itself shows the FDCs of icosahedral shells for various γ values deformed by a spherical tip of the same size as the shell. For lower values of γ , the FDC remains quite close to the harmonic spring prediction. For larger values of γ , the relation is increasingly nonlinear, and then develops the buckling discontinuity. The size of the discontinuity increases with increasing γ and the critical value of the indentation for the buckling discontinuity decreases. Figure 1a shows the shape of a shell with $\gamma = 1,200$ immediately after the buckling discontinuity. The stress contours are indicated. One of the 12 conical five-fold-symmetry sites of the icosahedral shell has buckled and inverted. In the buckled state, the shell is detached from the tip at the centre, which is not the case in the small-force regime. The five-fold-symmetry sites thus indeed seem to act as structural defects that trigger buckling. The discontinuity of the FDC of a spherical shell with the same elastic moduli takes place at a much larger indentation (see the inset of Fig. 1b).

How do the predictions of TST compare with the AFM nanoindentation experiments? For small applied forces, the measured FDC is indeed linear in many cases. Comparing the three-dimensional Young moduli (equation (2)) of various particles shows that sphere-like viruses that package their genome into preformed capsids, such as phage $\Phi 29$, phage λ , HSV1 (herpes simplex virus type 1) and MVM (minute virus of mice) have a Young modulus that is at least double that of sphere-like viruses that self-assemble around their genome such as CCMV and HBV (Table 1). The FvK numbers in Table 1 were, incidentally, not obtained by comparing with measured shell shapes but, instead, were estimated assuming the TST relation

$$\gamma = 12(1 - \nu^2) \left(\frac{R}{h} \right)^2 \quad (3)$$

with ν Poisson’s ratio. An interesting application is the use of TST to explain measured differences in spring constants of ‘nuclear’ and ‘viral’ HSV1 capsids^{65,66}. The latter are stiffer than the former because they possess an extra protein layer, the inner tegument. Using equation (2), and assuming that the E_{3D} values for the capsid and inner tegument are similar, it follows that this extra protein layer should have a thickness of ~ 0.8 nm (ref. 65), a prediction that is verifiable by electron microscopy.

For smaller viral particles, when the shell thickness h is not negligible compared with the radius R , TST is no longer expected to apply. The simplest extension is to use FEM to compute the FDC of a homogeneous elastic shell with a finite thickness. The elastic energy of a solid elastic sphere that is indented scales as $\zeta^{5/2}$, which is known as a ‘Hertzian’ response. The FDC of a thick-walled shell is expected to show, as a function of h , scaling

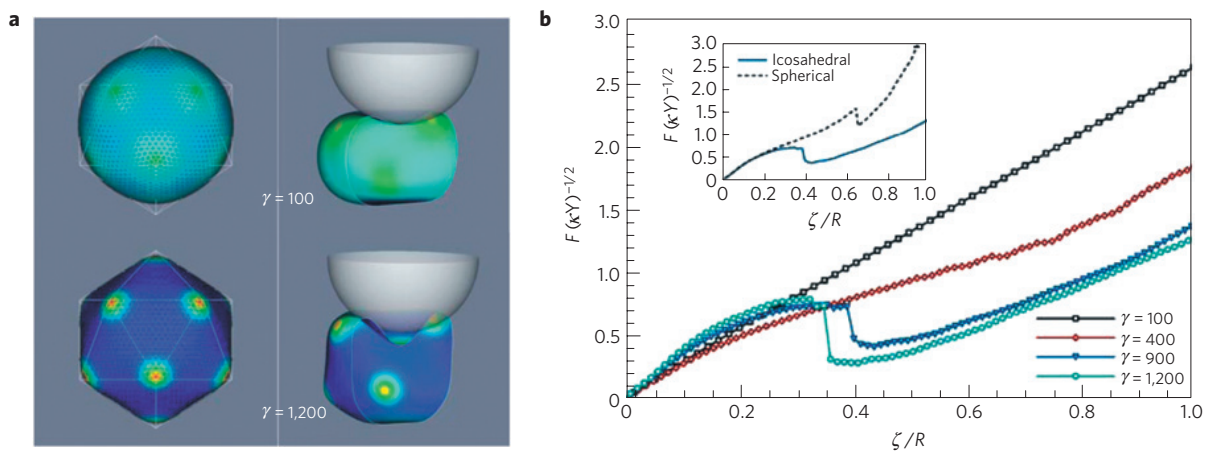


Figure 1 | FEM analysis of shell deformation. **a**, Shapes of icosahedral shells with $\gamma = 100$ and $\gamma = 1,200$. Undeformed shells (left) and shells that are deformed to 35% of their radius (right) are shown. The deformed shells are shown in a cutaway view and the $\gamma = 1,200$ shell has buckled, leading to the inversion of a five-fold apex. The strain energy due to stretching and bending is indicated by colour coding. **b**, FDC of icosahedral shells with isotropic elastic properties. The force F and the shell deformation ζ are expressed in dimensionless units. The graph shows that the FvK parameter γ determines whether a shell buckles. The inset compares FDCs on spherical and icosahedral shells for $\gamma = 900$. Reproduced with permission from ref. 77, © 2006 APS.

Table 1 | Geometrical and mechanical properties of viral shells/tubes.

	Radius* (nm)	Thickness* (nm)	Genome (encapsulation) [†]	Young's modulus (GPa)	FvK number [‡]	T number
$\Phi 29$ prohead	23.2 (ref. 70)	1.6	dsDNA (P)	1.8 (ref. 67)/4.5 (ref. 70)	2,100	Prolate
λ	29.5 (ref. 76)	1.8	dsDNA (P)	1.0 (ref. 76)	2,700	$T = 7$
HSV1	49.5 (ref. 65)	4	dsDNA (P)	1.0 (ref. 65)	1,500	$T = 16$
MVM	11.5 (ref. 68)	2	ssDNA (P)	1.25 (ref. 68)	350	$T = 1$
CCMV	11.8 (ref. 70)	2.8	ssRNA (S)	0.14 (ref. 71)/0.28 (ref. 70)/0.22 (ref. 72)	180	$T = 3$
HBV T3	11.9 (ref. 74)	2.4	ssRNA/DNA (S)	0.37 (ref. 74) / 0.26 (ref. 73)	250	$T = 3$
HBV T4	13.6 (ref. 74)	2.1	ssRNA/DNA (S)	0.36 (ref. 74) / 0.26 (ref. 73)	400	$T = 4$
TMV	5.5 (ref. 69)	7	ssRNA (S)	0.9/1.0 (ref. 69)	Cylindrical	Cylindrical

*Averaged shell radii (average of averaged outer and inner radius) and thicknesses are used. Phage $\Phi 29$ has a prolate shell, but has been approximated as a sphere. The shell radius and thickness of HSV1 and HBV are taken without the respective protrusions and spikes on the capsid surface.

[†]ss: single stranded, ds: double stranded. HBV self-assembles around an ssRNA genome, which is then retrotranscribed into DNA that is partially ss and partially ds. Encapsulation mode: P, packaging of genome into preformed capsids; S, self-assembly of capsid around genome.

[‡]The FvK number is calculated from equation (3), with $\nu = 0.4$ (ref. 70); rounded values are printed.

crossover from the TST result for larger applied forces to a nonlinear Hertzian-type FDC for smaller applied forces. FEM studies of the indentation of elastic shells by point forces^{67,68}, as well as by realistically shaped models for the AFM tip^{69–71}, were carried out. It was indeed observed that Hertzian nonlinearities occur at the onset of deformation of thick-shelled particles^{69,71}. The next step is to use information on the heterogeneous geometry of the viral particles available from X-ray diffraction and cryo-electron microscopy studies, while still maintaining a uniform elastic modulus. Such an approach was followed by Klug and co-workers to investigate CCMV and HBV (refs 72,73). By comparison with the measured FDC, a Young modulus of 0.22 GPa was found for CCMV, which happens to lie between the estimates obtained by the previous two methods^{70,71}. A comparable Young modulus, namely 0.26 GPa, was determined for HBV (ref. 73), which is a little lower than that obtained by using a TST approximation⁷⁴. Determining the Young modulus thus depends to some extent on the model that is used to analyse the FDC, as indicated in Table 1. Another example was a detailed FEM study of MVM that predicted stabilizing interactions between the encapsulated DNA and specific sites at the capsid interior (Fig. 2), which was later experimentally confirmed⁷⁵. Furthermore, the orientation-dependent indentation

behaviour of HBV was determined by comparing experiments with detailed FEM simulations⁷³. Table 1 summarizes mechanical and geometrical parameters of various viruses including the CK triangulation number T .

Reversible versus irreversible deformation

We now turn to the question of how the irreversible deformations of capsids can be described. The FDCs computed from elasticity theory are of course always reversible, though they may show hysteresis near buckling instabilities, but could a buckling instability seen in TST (or FEM) act as an indicator of fracture or some other form of irreversibility? This is actually the case for the failure of hollow macroscopic structures. First, recall that the critical deformation for the buckling instability is controlled by the FvK number. Buckling occurs at lower deformations for higher FvK numbers. Table 1 summarizes the approximate FvK numbers of a number of viruses. HSV1 capsids have an FvK number of $\sim 1,500$ and the empty capsids break at a relative deformation of $\sim 36\%$ of the radius⁶⁵. Prohead $\Phi 29$ and the empty phage λ have FvK numbers between 2,000 and 3,000. They should thus break at lower relative deformations than HSV1 and this is indeed the case: fracture takes place at a relative deformation that is 20–25% of the capsid radius⁷⁶.

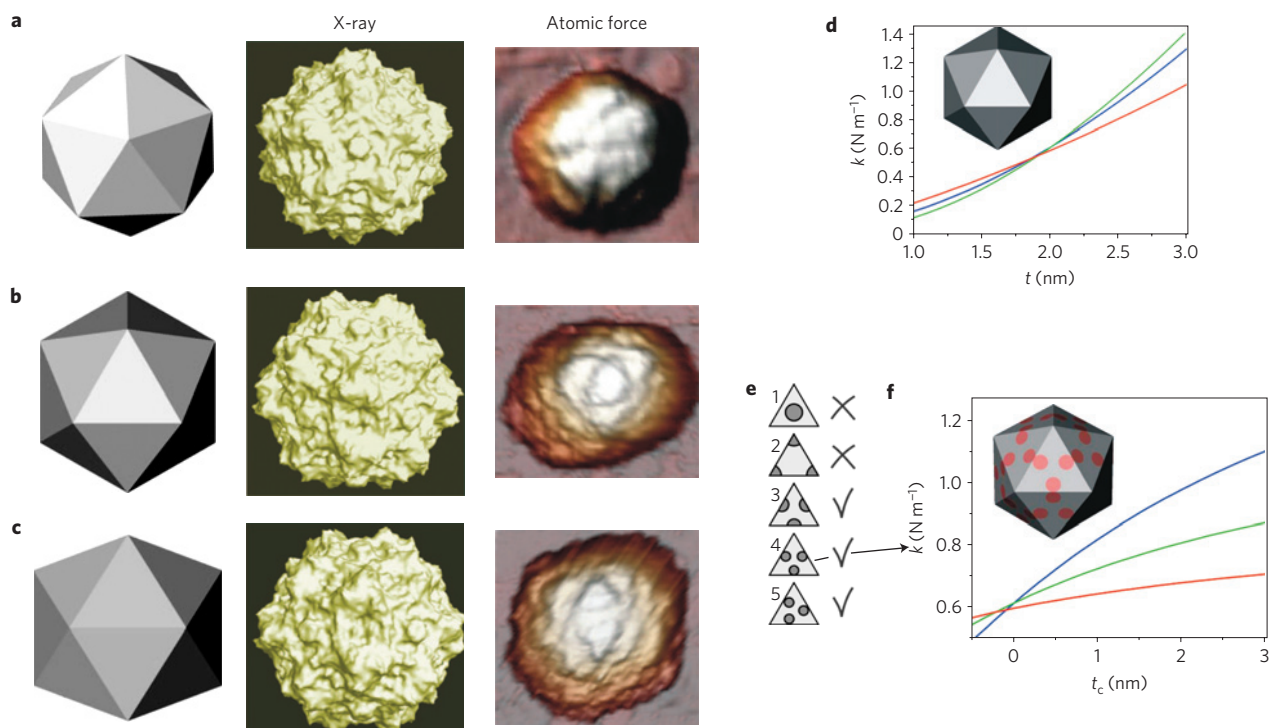


Figure 2 | Orientation dependence of MVM. a–c, From top to bottom: particles as seen along the five-, three- and two-fold symmetry axes. From left to right: schematic images of icosahedrons, reconstructions of MVM capsids, AFM images of MVM capsids. **d,** FEM analysis along the five-fold (red), three-fold (green) and two-fold (blue) symmetry axes as a function of shell thickness t . The experiments yield similar spring constants along all three axes of the empty particles (data not shown). These results match best with simulations for $t \sim 2$ nm. **e,** Reinforced shell models with patches of extra thickness t_c at various sites. Only Models 3–5 predict the correct anisotropic reinforcement of DNA-filled MVM capsids as observed experimentally. Importantly, the patches in these three models coincide roughly with the locations where ordered DNA is bound to the shell, whereas this does not coincide in Models 1 and 2. **f,** FEM analysis result for Model 4 in **e**. Reproduced with permission from ref. 68, © 2006 NAS, USA.

This at least is consistent with the notion that TST-type ‘inversion’ buckling instabilities mark irreversible fracture of viral shells.

The study of the fracture of CCMV viruses provides a revealing contrast between reversible and irreversible behaviour. At pH 5, CCMV fails after passing a critical indentation level⁷¹. In terms of TST, it behaves like a shell with an FvK number of ~ 900 (ref. 77). However, the same capsid at pH 6 exhibits a linear FDC all the way until it is completely flattened⁷⁷. The spring constant is significantly reduced and the capsid could be described as a shell with an FvK number of ~ 100 . Within TST, this can only be understood as a pronounced softening of the Young modulus induced by the pH change. This softening of the CCMV shell with increasing pH would make sense if a structural phase transition took place. In fact, a swelling transition does take place but only around pH 7. The morphologies of CCMV shells at pH 5 and pH 6 cannot be distinguished. Structural transitions of bulk systems are however often preceded by pre-transitional softening, as discussed earlier, and this may explain the softening of the CCMV shell for pH 5–6. Separately, these measurements indicate that, at least for small, thick-walled viruses such as CCMV, large changes in the elastic stiffness need not be reflected in the shell morphology. This means that it may not be appropriate to estimate the effective FvK number either by shape determination or by equation (3). Interestingly, experimental and simulated FDCs on the heavily structured shells of $T = 3$ and $T = 4$ HBV particles show a reasonably good fit, indicating that equation (3) can be used to estimate the FvK number of HBV capsids⁷³. However, a detailed analysis of the deformation behaviour of these particles also reveals that the FvK thin-shell elasticity model has its limitations in describing HBV capsids, as it does not properly capture the observed orientation dependence of indentation.

It seems likely that the irreversible failure of a shell is due to changes induced by the AFM tip in the pattern of the non-covalent chemical bonds that link the capsid proteins and that stabilize their secondary and tertiary structure. In single-molecule force spectroscopy, it is commonly observed that measured ‘fracture forces’ of bonds in actuality depend on the loading rate with which we probe the bond⁷⁸. CCMV follows this trend: the breaking force increases by $\sim 10\%$ for an increase of two orders of magnitude in loading rate, whereas it does not show a change in spring constant over this range⁷¹. Most of the measurements discussed in this review were made at loading rates of roughly 1 nN s^{-1} . Failure occurs normally over a relatively small range of relative deformations, typically about $28 \pm 8\%$ of the capsid radius^{65,79}. The average fracture force shows a larger range of values. In particular, empty CCMV capsids break at force levels of the order of 0.6 nN (ref. 71), empty phage λ particles at $\sim 0.8 \text{ nN}$ (ref. 76), prohead $\Phi 29$ at $\sim 1.5 \text{ nN}$ (ref. 76) and empty HSV-1 capsids at $\sim 6 \text{ nN}$ (ref. 65). Fracture is not the only form of irreversibility. For large deformations, FDCs can be irreversible without fracture, as is the case for HBV capsids⁸⁰. The form of the FDC suggests that in that case an effect akin to plastic deformation is taking place on a molecular scale. HBV irreversible deformations start around indentation levels of 60% of the HBV capsid radius⁷⁴, a much higher deformation than the buckling/fracture point of the more brittle capsids of phages $\Phi 29$ and λ and of HSV1. The plastic deformation of HBV capsids could be viewed as a form of ‘soft’ failure with a continuous but nonlinear indentation response resembling FDCs of particles with $100 < \gamma < 400$ (Fig. 1b).

Irreversible deformations of microscopic systems are fundamentally interesting. Dissociation of a hydrogen molecule is reversible

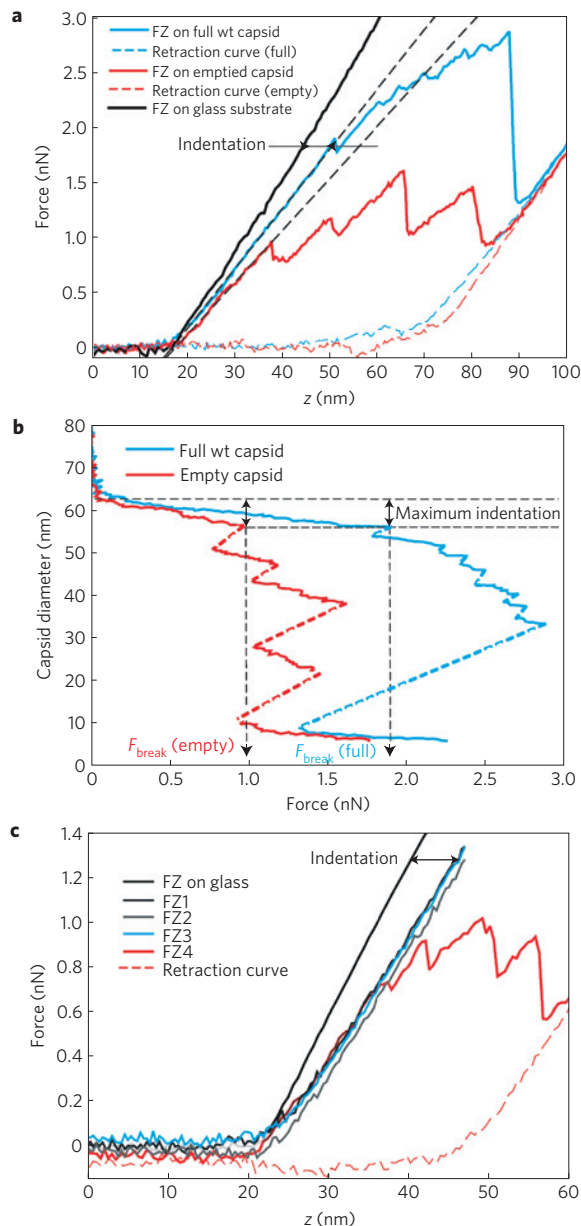


Figure 3 | Nanoindentation of phage λ . **a**, FZC on wild-type (wt; 100% DNA) and empty phage. The dashed black line shows the fit of the initial linear indentation regime. Both particles break in multiple steps. The difference of the FZC on the virus and FZC on the glass is denoted by ‘indentation’ and yields the FDC (see Box 2). **b**, These FDCs plotted as capsid height versus force. **c**, Material fatigue: after multiple deformations in the linear, reversible-indentation regime the shell breaks. Reproduced with permission from ref. 76, © 2007 NAS, USA.

but the forced unfolding of a protein can be irreversible, and materials scientists are deeply interested in ‘self-healing’ molecular structures. MD simulations can be used to study the stability and deformation of viral shells^{73,80–84}. The plastic deformation of HBV (refs 73,80) and the brittle failure of CCMV (ref. 84) have been studied by MD and compared with AFM nanoindentation experiments. Unlike TST, MD simulations can capture irreversibility. In particular, MD simulations exhibit the differences between successive indentation cycles that are observed experimentally⁸⁰. Plastic deformation of HBV was found to occur when highly deformed proteins established new interactions that remained intact when the load was

removed, at least over the simulation timescale. However, owing to the high computational demand of these simulations, the loading rates that were used had to be orders of magnitude higher than those used in experiment, even when coarse-graining methods were used. Because of the rate-dependence of molecular bond-fracture we mentioned above, quantitative comparisons remain challenging.

Apart from the TST-like abrupt shell failure at high deformations, it turns out that some particles will break on repetitive small deformations while remaining in the reversible elastic regime. This closely resembles the phenomenon of ‘fatigue’ that is familiar from the materials science of metals, except that here of course it occurs at the nanoscale level. It was, for example, shown that procapsids of phage $\Phi 29$, mature phage λ capsids (Fig. 3c) and MVM particles can bear repetitive, small deformations, but that repeated deformations finally lead to shell failure^{67,68,70}. The $\Phi 29$ proheads could be ‘gently tapped’ tens of times before the shell broke, but the other two broke after only a few deformation repetitions. In particular, damage to MVM occurred on average after seven indentations with a maximum force of 0.9 nN. This should be contrasted with the $T = 3$ and $T = 4$ shells of HBV that were highly resilient against repetitive deformations. No sign of fatigue was observed after pushing 35 times on the HBV capsids with a force of ~ 0.8 nN (ref. 74). The phenomenon of capsid fatigue is thus quite specific to the particular species of virus. This shows that, despite the structural uniformity of spherical capsids, there is a wide range of materials properties. For macroscopic structures, fatigue is associated with the stress-induced growth of lines of broken bonds (known as ‘Griffith cracks’)⁸⁵. Simple models show that crack formation is expected as well for viral shells when the protein–protein bond strength is reduced⁸⁶.

Influence of the genome on capsid mechanical properties

Until now we have mostly discussed the mechanical properties of empty shells. Now we turn our attention to the changes in the mechanical properties of viral shells that take place when they enclose DNA or RNA genome molecules. The density of the close-packed genome material inside the water-permeable shells can be so high that it generates significant osmotic pressures (Π), in the range of tens of atmospheres. In turn, this pressure generates a non-specific tension τ along the shell according to Laplace’s law $\Pi = 2\tau/R$ (for a spherical shell), which increases the shell’s spring constant (see equation (1)). According to TST, non-specific stiffening should start to change the spring constant for pressures in excess of $\Pi_c \sim (I_B Y/R^2)$. This is about an order of magnitude larger than actual osmotic pressures — using our earlier estimates for the two-dimensional Young modulus Y — so pressure-induced stiffening is expected to be a modest effect⁵³.

The impact of osmotic pressure on the non-specific shell stiffening was investigated for phage λ . By comparing the mechanical properties of empty and full particles with mutant particles that had a shorter genome (78 and 94% of the wild-type genome), it was observed that the presence of the dsDNA in phage λ was indeed noticeable only at very high genome densities⁷⁶ (Fig. 3). Similar experiments were carried out on HSV1, a dsDNA virus that exhibits structural analogies to the tailed dsDNA phages⁸⁷. The stiffness measurement of full and empty HSV1 capsids showed no mechanical difference between the particles⁶⁵. Presumably the increased stiffness due to the DNA-induced osmotic pressure even at the maximal packaging density in HSV1 is too small compared with the intrinsic stiffness of the capsid shell. Yet, in other cases, genome-induced shell stiffening effects are surprisingly pronounced. A remarkable case is the stiffening of the icosahedral capsids of MVM that takes place after the packaging of the viral ssDNA (Fig. 2). The stiffening is anisotropic: the empty MVM capsids have the same spring constants when the

virus presents a two-fold, a three-fold or a five-fold symmetry site to the probe. Packaging of the viral genome increases the spring constant with $\sim 40\%$ along the three-fold axis and $\sim 140\%$ along the two-fold axis⁶⁸. The spring constant along the five-fold axis remains nearly unaffected by the genome packaging. This symmetry-axis-dependent reinforcement presumably is due to specific interactions between the viral genome and portions of the inner capsid wall⁷⁵ with different symmetry that locally increase the bending energy κ of TST (see equation (1)). As the five-fold sites are likely to be the ports of entry and exit of the genome, it would seem reasonable that attractive interactions between genome and capsid are weaker at the five-fold sites. Finally, CCMV capsids can assemble either empty or with enclosed viral ssRNA. The spring constant and fracture force increased by $\sim 30\%$ when the genome was incorporated⁷¹ but there was no symmetry-specific reinforcement. The increased stability and stiffness could be due to the generic affinity between the positively charged N termini of CCMV capsid proteins and the RNA, which increases the effective shell thickness.

Role of mechanical virology in biology and biotechnology

We have seen that viral self-assembly, stability and deformation response can be usefully described by physical arguments based on statistical mechanics and continuum elastic theory, and that concepts borrowed from macroscopic materials science seem to translate remarkably well to these nanoscale assemblies. Now we would like to focus on the question of how we can apply these experiments and descriptions to biology and biotechnology. Nanoindentation experiments on the retroviruses murine leukaemia virus and HIV show that the viral particles soften during maturation^{88,89}. This softening is striking — phages for instance are expected to stiffen during maturation — but it is clearly linked to viral infectivity. Soft, mature HIV particles enter cells much more efficiently than stiff, immature particles. Controls in which the viral envelope protein of the immature HIV particles was truncated decreased the stiffness of the immature particles to values similar to that of the mature particles. As a result, the entry efficiency of the immature particles was greatly increased. This shows a direct link between mechanical properties and infectivity. Another example of a link between mechanical virology and biology is provided by the nanoindentation experiments on herpes particles (see Fig. B3). On purification of HSV1 capsids from the nuclei of infected cells, three different types of nucleocapsid are obtained: the scaffold-containing B capsids, the empty A capsids and the DNA-containing C capsids. All three capsid types have a mature shell and, until recently, it was unclear whether there were significant differences between the shells of these particles. Nanoindentation measurements have shown that the A and C capsids have mechanical properties that are indistinguishable, but B capsids break at a much lower force than the other two types⁶⁵. Apparently, scaffold expulsion during particle maturation and subsequent genome packaging trigger a stabilization of the viral shell, in particular around the 12 icosahedral vertices. This stabilization might be essential for virus survival during microtubule-mediated transport shuttling the particle between the nucleus and the cell membrane.

The example of the change in material properties of immature HIV particles indicates that the mechanical properties of viral shells can be altered dramatically by manipulating the viral proteins. The interactions between the packaged DNA and the inner capsid wall of MVM can be inhibited by removal of specific amino-acid side chains of the MVM capsid protein⁷⁵. This, in turn, reduces the spring constant of the particle to the point that it becomes indistinguishable from that of an empty capsid. The substitution of even a single amino acid can affect the mechanical properties

of viral shells: a single point mutation of the capsid protein of CCMV has been shown to significantly increase both the spring constant and the fracture strength⁷¹. It is also possible to remove specific structural subunits of the viral shell without disrupting the overall capsid structure. An example of this is the removal of the pentons of HSV1 capsids by treatment with 2.0 M GuHCl (ref. 90). The $T = 16$ capsid retains an icosahedral shape, but the five-fold-symmetry sites are replaced by holes. Shells of this type, which are called ‘whiffle balls’, are also encountered for HK97 mutants⁹¹. Simple elastic models of whiffle-ball shells show that their effective FvK number is effectively lowered compared with the fully closed shell and that they are much softer⁸⁶. Nanoindentation measurements have confirmed the remarkable material properties of these particles. The spring constant and breaking force of empty as well as DNA-filled HSV1 capsids were reduced by roughly 50% on GuHCl treatment⁶⁵.

In conclusion, physics provides a useful framework to describe both viral self-assembly and the mechanics of viral shells. Recently developed TST, FEM and MD methods are expected to provide further insights into the ‘molecular mechanics’ of viruses and support the development of functional viral nanoparticles for use in technology and medicine.

References

- Fischlechner, M. & Donath, E. Viruses as building blocks for materials and devices. *Angew. Chem. Int. Ed.* **46**, 3184–3193 (2007).
- Singh, P., Gonzalez, M. J. & Manchester, M. Viruses and their uses in nanotechnology. *Drug Dev. Res.* **67**, 23–41 (2006).
- Lee, Y. J. *et al.* Fabricating genetically engineered high-power lithium-ion batteries using multiple virus genes. *Science* **324**, 1051–1055 (2009).
- Tseng, R. J., Tsai, C. L., Ma, L. P. & Ouyang, J. Y. Digital memory device based on tobacco mosaic virus conjugated with nanoparticles. *Nature Nanotechnol.* **1**, 72–77 (2006).
- Everts, M. *et al.* Covalently linked Au nanoparticles to a viral vector: Potential for combined photothermal and gene cancer therapy. *Nano Lett.* **6**, 587–591 (2006).
- Douglas, T. & Young, M. Host–guest encapsulation of materials by assembled virus protein cages. *Nature* **393**, 152–155 (1998).
- Parato, K. A., Senger, D., Forsyth, P. A. J. & Bell, J. C. Recent progress in the battle between oncolytic viruses and tumours. *Nature Rev. Cancer* **5**, 965–976 (2005).
- Kay, M. A., Glorioso, J. C. & Naldini, L. Viral vectors for gene therapy: The art of turning infectious agents into vehicles of therapeutics. *Nature Med.* **7**, 33–40 (2001).
- Summers, W. C. Bacteriophage therapy. *Annu. Rev. Microbiol.* **55**, 437–451 (2001).
- Stockley, P. & Twarock, R. (eds) *Emerging Topics in Physical Virology* (Imperial College, 2010).
- Bruinsma, R. F., Gelbart, W. M., Reguera, D., Rudnick, J. & Zandi, R. Viral self-assembly as a thermodynamic process. *Phys. Rev. Lett.* **90**, 248101 (2003).
- Zlotnick, A. Theoretical aspects of virus capsid assembly. *J. Mol. Recognit.* **18**, 479–490 (2005).
- Gelbart, W. M. & Knobler, C. M. Pressurized viruses. *Science* **323**, 1682–1683 (2009).
- Roos, W. H., Ivanovska, I. L., Evilevitch, A. & Wuite, G. J. L. Viral capsids: Mechanical characteristics, genome packaging and delivery mechanisms. *Cell. Mol. Life Sci.* **64**, 1484–1497 (2007).
- Sun, S. Y., Rao, V. B. & Rossmann, M. G. Genome packaging in viruses. *Curr. Opin. Struct. Biol.* **20**, 114–120 (2010).
- Baumeister, W. & Steven, A. C. Macromolecular electron microscopy in the era of structural genomics. *Trends Biochem. Sci.* **25**, 624–631 (2000).
- Natarajan, P. *et al.* Exploring icosahedral virus structures with VIPER. *Nature Rev. Microbiol.* **3**, 809–817 (2005).
- Fraenkel-Conrat, H. & Williams, R. C. Reconstitution of active tobacco mosaic virus from its inactive protein and nucleic acid components. *Proc. Natl Acad. Sci. USA* **41**, 690–698 (1955).
- Butler, P. J. G. & Klug, A. Assembly of a virus. *Sci. Am.* **239**, 62–69 (1978).
- Bancroft, J. B., Hills, G. J. & Markham, R. A study of self-assembly process in a small spherical virus—formation of organized structures from protein subunits *in vitro*. *Virology* **31**, 354–379 (1967).
- Klug, A. The tobacco mosaic virus particle: Structure and assembly. *Phil. Trans. R. Soc. Lond. B* **354**, 531–535 (1999).

22. Caspar, D. L. D. Assembly and stability of the tobacco mosaic virus particle. *Adv. Protein Chem.* **18**, 37–121 (1963).
23. Kegel, W. K. & van der Schoot, P. Physical regulation of the self-assembly of tobacco mosaic virus coat protein. *Biophys. J.* **91**, 1501–1512 (2006).
24. Bruinsma, R. F. Physics of RNA and viral assembly. *Eur. Phys. J. E* **19**, 303–310 (2006).
25. Tang, L. *et al.* The structure of Pariaquito virus reveals a dodecahedral cage of duplex RNA. *Nature Struct. Biol.* **8**, 77–83 (2001).
26. Johnson, J. M. *et al.* Regulating self-assembly of spherical oligomers. *Nano Lett.* **5**, 765–770 (2005).
27. Ceres, P. & Zlotnick, A. Weak protein–protein interactions are sufficient to drive assembly of hepatitis B virus capsids. *Biochemistry* **41**, 11525–11531 (2002).
28. Safran, S. *Statistical Thermodynamics of Surfaces, Interfaces, and Membranes*; *Frontiers in Physics* (Westview Press, 2003).
29. Singh, S. & Zlotnick, A. Observed hysteresis of virus capsid disassembly is implicit in kinetic models of assembly. *J. Biol. Chem.* **278**, 18249–18255 (2003).
30. Morozov, A. Y., Bruinsma, R. F. & Rudnick, J. Assembly of viruses and the pseudo-law of mass action. *J. Chem. Phys.* **131**, 155101 (2009).
31. Endres, D. & Zlotnick, A. Model-based analysis of assembly kinetics for virus capsids or other spherical polymers. *Biophys. J.* **83**, 1217–1230 (2002).
32. Berthet-Colominas, C., Cuillel, M., Koch, M. H. J., Vachette, P. & Jacrot, B. Kinetic-study of the self-assembly of bromo mosaic-virus capsid. *Eur. Biophys. J. Biophys. Lett.* **15**, 159–168 (1987).
33. Prevelige, P. E., Thomas, D. & King, J. Nucleation and growth phases in the polymerization of coat and scaffolding subunits into icosahedral procapsid shells. *Biophys. J.* **64**, 824–835 (1993).
34. Choi, Y. G., Dreher, T. W. & Rao, A. L. N. tRNA elements mediate the assembly of an icosahedral RNA virus. *Proc. Natl Acad. Sci. USA* **99**, 655–660 (2002).
35. Zlotnick, A., Aldrich, R., Johnson, J. M., Ceres, P. & Young, M. J. Mechanism of capsid assembly for an icosahedral plant virus. *Virology* **277**, 450–456 (2000).
36. Casini, G. L., Graham, D., Heine, D., Garcea, R. L. & Wu, D. T. *In vitro* papillomavirus capsid assembly analyzed by light scattering. *Virology* **325**, 320–327 (2004).
37. Nguyen, T. T., Bruinsma, R. F. & Gelbart, W. M. Continuum theory of retroviral capsids. *Phys. Rev. Lett.* **96**, 078102 (2006).
38. Endres, D., Miyahara, M., Moisan, P. & Zlotnick, A. A reaction landscape identifies the intermediates critical for self-assembly of virus capsids and other polyhedral structures. *Protein Sci.* **14**, 1518–1525 (2005).
39. Zhang, T. Q. & Schwartz, R. Simulation study of the contribution of oligomer/oligomer binding to capsid assembly kinetics. *Biophys. J.* **90**, 57–64 (2006).
40. Hemberg, M., Yaliraki, S. N. & Barahona, M. Stochastic kinetics of viral capsid assembly based on detailed protein structures. *Biophys. J.* **90**, 3029–3042 (2006).
41. Hagan, M. F. & Chandler, D. Dynamic pathways for viral capsid assembly. *Biophys. J.* **91**, 42–54 (2006).
42. Hicks, S. D. & Henley, C. L. Irreversible growth model for virus capsid assembly. *Phys. Rev. E* **74**, 031912 (2006).
43. Nguyen, H. D., Reddy, V. S. & Brooks, C. L. Invariant polymorphism in virus capsid assembly. *J. Am. Chem. Soc.* **131**, 2606–2614 (2009).
44. Rapaport, D. C. Role of reversibility in viral capsid growth: A paradigm for self-assembly. *Phys. Rev. Lett.* **101**, 186101 (2008).
45. Berger, B., Shor, P. W., Tuckerkellogg, L. & King, J. Local rule-based theory of virus shell assembly. *Proc. Natl Acad. Sci. USA* **91**, 7732–7736 (1994).
46. Zandi, R., Reguera, D., Bruinsma, R. F., Gelbart, W. M. & Rudnick, J. Origin of icosahedral symmetry in viruses. *Proc. Natl Acad. Sci. USA* **101**, 15556–15560 (2004).
47. Chen, T., Zhang, Z. L. & Glotzer, S. C. A precise packing sequence for self-assembled convex structures. *Proc. Natl Acad. Sci. USA* **104**, 717–722 (2007).
48. Nguyen, T. T., Bruinsma, R. F. & Gelbart, W. M. Elasticity theory and shape transitions of viral shells. *Phys. Rev. E* **72**, 051923 (2005).
49. Moody, M. F. Geometry of phage head construction. *J. Mol. Biol.* **293**, 401–433 (1999).
50. Chen, T. & Glotzer, S. C. Simulation studies of a phenomenological model for elongated virus capsid formation. *Phys. Rev. E* **75**, 051504 (2007).
51. Luque, A., Zandi, R. & Reguera, D. Optimal architectures of elongated viruses. *Proc. Natl Acad. Sci. USA* **107**, 5323–5328 (2010).
52. Zhang, R. & Nguyen, T. T. Model of human immunodeficiency virus budding and self-assembly: Role of the cell membrane. *Phys. Rev. E* **78**, 051903 (2008).
53. Guerin, T. & Bruinsma, R. Theory of conformational transitions of viral shells. *Phys. Rev. E* **76**, 061911 (2007).
54. Wikoff, W. R. *et al.* Topologically linked protein rings in the bacteriophage HK97 capsid. *Science* **289**, 2129–2133 (2000).
55. Tama, F. & Brooks, C. L. The mechanism and pathway of pH induced swelling in cowpea chlorotic mottle virus. *J. Mol. Biol.* **318**, 733–747 (2002).
56. Tama, F. & Brooks, C. L. Diversity and identity of mechanical properties of icosahedral viral capsids studied with elastic network normal mode analysis. *J. Mol. Biol.* **345**, 299–314 (2005).
57. Widom, M., Lidmar, J. & Nelson, D. R. Soft modes near the buckling transition of icosahedral shells. *Phys. Rev. E* **76**, 031911 (2007).
58. Yang, Z., Bahar, I. & Widom, M. Vibrational dynamics of icosahedrally symmetric biomolecular assemblies compared with predictions based on continuum elasticity. *Biophys. J.* **96**, 4438–4448 (2009).
59. Anderson, T. F., Rappaport, C. & Muscatine, N. A. On the structure and osmotic properties of phage particles. *Ann. Inst. Pasteur* **84**, 5–15 (1953).
60. Stephanidis, B., Adichtchev, S., Gouet, P., McPherson, A. & Mermet, A. Elastic properties of viruses. *Biophys. J.* **93**, 1354–1359 (2007).
61. Hartschuh, R. D. *et al.* How rigid are viruses. *Phys. Rev. E* **78**, 021907 (2008).
62. Smith, D. E. *et al.* The bacteriophage phi 29 portal motor can package DNA against a large internal force. *Nature* **413**, 748–752 (2001).
63. Evilevitch, A., Lavelle, L., Knobler, C. M., Raspaud, E. & Gelbart, W. M. Osmotic pressure inhibition of DNA ejection from phage. *Proc. Natl Acad. Sci. USA* **100**, 9292–9295 (2003).
64. Lidmar, J., Mirny, L. & Nelson, D. R. Virus shapes and buckling transitions in spherical shells. *Phys. Rev. E* **68**, 051910 (2003).
65. Roos, W. H. E. Scaffold expulsion and genome packaging trigger stabilization of herpes simplex virus capsids. *Proc. Natl Acad. Sci. USA* **106**, 9673–9678 (2009).
66. Liashkovich, I. *et al.* Exceptional mechanical and structural stability of HSV-1 unveiled with fluid atomic force microscopy. *J. Cell Sci.* **121**, 2287–2292 (2008).
67. Ivanovska, I. L. *et al.* Bacteriophage capsids: Tough nanoshells with complex elastic properties. *Proc. Natl Acad. Sci. USA* **101**, 7600–7605 (2004).
68. Carrasco, C. *et al.* DNA-mediated anisotropic mechanical reinforcement of a virus. *Proc. Natl Acad. Sci. USA* **103**, 13706–13711 (2006).
69. Zhao, Y., Ge, Z. B. & Fang, J. Y. Elastic modulus of viral nanotubes. *Phys. Rev. E* **78**, 031914 (2008).
70. Gibbons, M. M. & Klug, W. S. Nonlinear finite-element analysis of nanoindentation of viral capsids. *Phys. Rev. E* **75**, 031901 (2007).
71. Michel, J. P. *et al.* Nanoindentation studies of full and empty viral capsids and the effects of capsid protein mutations on elasticity and strength. *Proc. Natl Acad. Sci. USA* **103**, 6184–6189 (2006).
72. Gibbons, M. M. & Klug, W. S. Influence of nonuniform geometry on nanoindentation of viral capsids. *Biophys. J.* **95**, 3640–3649 (2008).
73. Roos, W. H. *et al.* Squeezing protein shells: how continuum elastic models, molecular dynamics simulations and experiments coalesce at the nanoscale. *Biophys. J.* **99**, 1175–1181 (2010).
74. Utrecht, C. *et al.* High-resolution mass spectrometry of viral assemblies: Molecular composition and stability of dimorphic hepatitis B virus capsids. *Proc. Natl Acad. Sci. USA* **105**, 9216–9220 (2008).
75. Carrasco, C., Castellanos, M., de Pablo, P. J. & Mateu, M. G. Manipulation of the mechanical properties of a virus by protein engineering. *Proc. Natl Acad. Sci. USA* **105**, 4150–4155 (2008).
76. Ivanovska, I., Wuite, G., Jonsson, B. & Evilevitch, A. Internal DNA pressure modifies stability of WT phage. *Proc. Natl Acad. Sci. USA* **104**, 9603–9608 (2007).
77. Klug, W. S. *et al.* Failure of viral shells. *Phys. Rev. Lett.* **97**, 228101 (2006).
78. Evans, E. & Ritchie, K. Dynamic strength of molecular adhesion bonds. *Biophys. J.* **72**, 1541–1555 (1997).
79. Roos, W. H. & Wuite, G. J. L. Nanoindentation studies reveal material properties of viruses. *Adv. Mater.* **21**, 1187–1192 (2009).
80. Arkhipov, A., Roos, W. H., Wuite, G. J. & Schulten, K. Elucidating the mechanism behind irreversible deformation of viral capsids. *Biophys. J.* **97**, 2061–2069 (2009).
81. Freddolino, P. L., Arkhipov, A. S., Larson, S. B., McPherson, A. & Schulten, K. Molecular dynamics simulations of the complete satellite tobacco mosaic virus. *Structure* **14**, 437–449 (2006).
82. Arkhipov, A., Freddolino, P. L. & Schulten, K. Stability and dynamics of virus capsids described by coarse-grained modeling. *Structure* **14**, 1767–1777 (2006).
83. Zink, M. & Grubmuller, H. Mechanical properties of the icosahedral shell of southern bean mosaic virus: A molecular dynamics study. *Biophys. J.* **96**, 1350–1363 (2009).
84. Cieplak, M. & Robbins, M. O. Nanoindentation of virus capsids in a molecular model. *J. Chem. Phys.* **132**, 015101 (2010).
85. Landau, L. D. & Lifshitz, E. M. *Theory of Elasticity* 3rd edn (Elsevier, 1986).
86. Morozov, A., Rudnick, J., Bruinsma, R. & Klug, W. in *Emerging Topics in Physical Virology* (eds Stockley, P. & Twarock, R.) (Imperial College, 2010).
87. Baker, M. L., Jiang, W., Rixon, F. J. & Chiu, W. Common ancestry of herpesviruses and tailed DNA bacteriophages. *J. Virol.* **79**, 14967–14970 (2005).

88. Kol, N. *et al.* Mechanical properties of murine leukemia virus particles: Effect of maturation. *Biophys. J.* **91**, 767–774 (2006).
89. Kol, N. *et al.* A stiffness switch in human immunodeficiency virus. *Biophys. J.* **92**, 1777–1783 (2007).
90. Newcomb, W. W. & Brown, J. C. Structure of the herpes-simplex virus capsid—effects of extraction with guanidine-hydrochloride and partial reconstitution of extracted capsids. *J. Virol.* **65**, 613–620 (1991).
91. Li, Y. Y. *et al.* Control of virus assembly: HK97 ‘Whiffleball’ mutant capsids without pentons. *J. Mol. Biol.* **348**, 167–182 (2005).
92. Zlotnick, A. Viruses and the physics of soft condensed matter. *Proc. Natl Acad. Sci. USA* **101**, 15549–15550 (2004).
93. Caspar, D. L. D. & Klug, A. Physical principles in construction of regular viruses. *Cold Spring Harbor Symp. Quant. Biol.* **27**, 1–24 (1962).
94. Johnson, J. E. & Speir, J. A. Quasi-equivalent viruses: A paradigm for protein assemblies. *J. Mol. Biol.* **269**, 665–675 (1997).
95. Crick, F. H. C. & Watson, J. D. Structure of small viruses. *Nature* **177**, 473–475 (1956).
96. Kasas, S. & Dietler, G. Probing nanomechanical properties from biomolecules to living cells. *Pflugers Arch.* **456**, 13–27 (2008).
97. Radmacher, M., Fritz, M., Kacher, C. M., Cleveland, J. P. & Hansma, P. K. Measuring the viscoelastic properties of human platelets with the atomic force microscope. *Biophys. J.* **70**, 556–567 (1996).
98. Sen, S., Subramanian, S. & Discher, D. E. Indentation and adhesive probing of a cell membrane with AFM: Theoretical model and experiments. *Biophys. J.* **89**, 3203–3213 (2005).
99. Vinckier, A., Dumortier, C., Engelborghs, Y. & Hellemans, L. Dynamical and mechanical study of immobilized microtubules with atomic force microscopy. *J. Vac. Sci. Technol. B* **14**, 1427–1431 (1996).
100. de Pablo, P. J., Schaap, I. A. T., MacKintosh, F. C. & Schmidt, C. F. Deformation and collapse of microtubules on the nanometer scale. *Phys. Rev. Lett.* **91**, 098101 (2003).
101. Kol, N. *et al.* Self-assembled peptide nanotubes are uniquely rigid bioinspired supramolecular structures. *Nano Lett.* **5**, 1343–1346 (2005).
102. Kuznetsov, Y. G., Malkin, A. J., Lucas, R. W., Plomp, M. & McPherson, A. Imaging of viruses by atomic force microscopy. *J. Gen. Virol.* **82**, 2025–2034 (2001).
103. Baclayon, M., Wuite, G. J. L. & Roos, W. H. Imaging and manipulation of single viruses by atomic force microscopy. *Soft Matter* doi:10.1039/b923992h (2010, in the press).
104. Putman, C. A. J., Vanderwerf, K. O., Degrooth, B. G., Vanhulst, N. F. & Greve, J. Tapping mode atomic-force microscopy in liquid. *Appl. Phys. Lett.* **64**, 2454–2456 (1994).
105. Moreno-Herrero, F. *et al.* Scanning force microscopy jumping and tapping modes in liquids. *Appl. Phys. Lett.* **81**, 2620–2622 (2002).

Acknowledgements

G.J.L.W. would like to acknowledge support by the Nederlandse Organisatie voor Wetenschappelijk Onderzoek in a CW-ECHO and a VICI grant, and support by the Stichting voor Fundamenteel Onderzoek der Materie under the ‘Physics of the genome’ research programme. R.B. would like to thank the NSF-DMR for support under Grant 0704274.

Additional information

The authors declare no competing financial interests. Reprints and permissions information is available online at <http://npg.nature.com/reprintsandpermissions>. Correspondence and requests for materials should be addressed to W.H.R. or G.J.L.W.